

Water-in-Salt Battery Electrolyte for High-Voltage Supercapacitors: A Fundamental Study on Biomass and Carbon Fiber Electrodes

To cite this article: Changmin Shi et al 2024 J. Electrochem. Soc. 171 110526

View the article online for updates and enhancements.

You may also like

- Review-Understanding Thermal Runaway in Lithium-Ion Batteries: Trigger, Mechanism, and Early Warning Strategies Chenchen Liu, Hai Dai, Danyang Wang et
- Lithium Plating at the Cell Edge Induced by Anode Overhang during Cycling in Lithium-Ion Batteries: Part II. Simulation and Experimental Validation

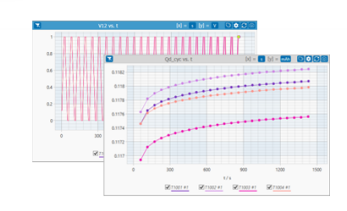
 F. F. Oehler, T. Roth, A. Frank et al.
- Thermodynamic Modeling of Point Defects in Triple Conducting Perovskite Ba_{0.95}La_{0.05}FeO₃ with Incorporation of the Hydride Defect Formation Reaction for Solid Oxide Cells Yueh-Lin Lee, Yuhua Duan, Dan C. Sorescu et al.

PAT-Tester-x-8 Potentiostat: Modular Solution for Electrochemical Testing!



- **✓** Flexible Setup with up to 8 Independent Test Channels! Each with a fully equipped Potentiostat, Galvanostat and EIS!
- ✓ Perfect Choice for Small-Scale and Special Purpose Testing! Suited for all 3-electrode, optical, dilatometry or force test cells from EL-CELL.
- ✓ Complete Solution with Extensive Software! Plan, conduct and analyze experiments with EL-Software.
- ✓ Small Footprint, Easy to Setup and Operate! Usable inside a glove box. Full multi-user, multi-device control via LAN.







Contact us:

- +49 40 79012-734
- sales@el-cell.com
- www.el-cell.com



Journal of The Electrochemical Society, 2024 171 110526
1945-7111/2024/171(11)/110526/6/\$40.00 © 2024 The Electrochemical Society ("ECS"). Published on behalf of ECS by IOP Publishing Limited. All rights, including for text and data mining, AI training, and similar technologies, are reserved.





Water-in-Salt Battery Electrolyte for High-Voltage Supercapacitors: A Fundamental Study on Biomass and Carbon Fiber Electrodes

W. Sheldon^{1,**},z

In this study, we investigated the use of a water-in-salt electrolyte (WiSE) for enhancing the performance of carbon-based supercapacitor electrodes. The all-biomass electrode and a peroxyacetyl nitrate-derived porous carbon fiber electrode (PPCF) were chosen as two examples for evaluating their electrochemical performance. WiSE provides a stable wide voltage window of 3 V, effectively inhibits undesirable water-splitting reactions. The presence of pseudocapacitance behavior, as evidenced by cyclic voltammetry scans, contributed to higher charge storage capacity. As a result, a high areal energy density and power density of 2.2 mWh cm⁻² and 11.7 mW cm⁻² were achieved for the all-biomass electrode, and a high areal energy density and power density of 0.4 mWh cm⁻² and 12.1 mW cm⁻² were achieved for the PPCF electrode. Overall, when coupled with carbon-based electrodes WiSE shows great promise for high-voltage supercapacitor applications, providing a balance between charge storage kinetics and interface stability.

© 2024 The Electrochemical Society ("ECS"). Published on behalf of ECS by IOP Publishing Limited. All rights, including for text and data mining, AI training, and similar technologies, are reserved. [DOI: 10.1149/1945-7111/ad92e0]

Manuscript submitted September 18, 2024; revised manuscript received November 6, 2024. Published November 27, 2024.

Supplementary material for this article is available online

In addition to batteries, the growing demand for efficient energy storage solutions has driven extensive research into supercapacitors, known for their high power density and long cycle life. 1-4 This makes supercapacitors a promising candidate for applications requiring quick bursts of energy, such as in power grids, electric vehicles, and portable electronic devices.⁵

Conventional supercapacitors rely on aqueous or organic electrolytes, each with distinct advantages and limitations. 9,10 Aqueous electrolytes offer high ionic conductivity and safety but are limited by a narrow voltage window due to the electrolysis of water, which typically restricts the cell voltage to about 1.2 V or even lower. 11,12 Organic electrolytes, while providing a wider voltage window (up to 3.75 V), ¹³ suffer from lower ionic conductivity, higher cost, and potential safety concerns due to flammability. ^{14–17} To overcome these limitations, recent advancements have focused on developing novel electrolytes that combine the benefits of both aqueous and organic systems.

One promising development in this field is the water-in-salt electrolyte (WiSE), which significantly expands the electrochemical stability window of aqueous electrolytes (up to 3 V). 18-20 WiSE consists of highly concentrated salt solutions that suppress water activity, thus inhibiting water-splitting reactions and allowing for stable operation at voltages beyond water electrolysis. This unique property has made WiSE an attractive candidate for high-voltage supercapacitor applications.

This study explores the use of WiSE to enhance the electrochemical performance, including areal energy density, power density and cycling stability, of carbon-based supercapacitor electrodes. We specifically investigate two types of electrodes: an all-biomass electrode and a peroxyacetyl nitrate (PAN)-derived porous carbon fiber (PPCF) electrode that developed by us. 21,22 The all-biomass electrode, derived from sustainable sources, offers an environmentally friendly and cost-effective alternative to traditional carbon materials. The PPCF electrode, prepared through electrospinning and subsequent thermal treatments, provides a high specific surface area (SSA) and highly porous structure, making it an excellent electrode candidate for high-performance supercapacitors.

We assessed the effectiveness of WiSE in preventing undesirable water-splitting reactions and supporting pseudocapacitance behavior. Furthermore, our results demonstrate that WiSE not only expands the voltage window but also contributes to high areal energy and power densities, thus enhancing the overall performance of supercapacitors. Despite the higher areal specific resistance (ASR) observed with WiSE, the electrodes, particularly the all-biomass candidate, showed excellent cycling stability and maintained high discharge capacitance over extended cycles. This study highlights the potential of WiSE in developing high-voltage supercapacitors with improved energy storage capabilities. The insights gained from this research could pave the way for the design of next-generation supercapacitors, balancing the trade-offs between charge storage kinetics and interface stability.

Experimental

Materials preparations.—The biochar wafer electrodes were produced from a proprietary blend of plant material (grasses, woody biomass) which was dried, pulverized, pressed into a shallow cylindrical mold which was placed in a torrefaction oven for charring. The resulting disc-shaped biochar wafers were removed from the mold and the biochar was then activated via immersion in a proprietary aqueous solution, after which the biochar wafers were heat-dried. For the PPCF electrode, PAN (Mwt. 15,000 g mol⁻¹ Sigma Aldrich) in dimethylformamide (99.5%, Fisher Scientific) was transferred to a syringe equipped with a 27-gauge needle. Electrospinning was conducted at a voltage of 15 kV. To enhance the conductivity and porosity of the PAN mesh, it was subjected to a series of thermal treatments, including stabilization, carbonization, and activation. The tubular furnace (GSL 1600X, MTI Corporation) was used for all thermal treatments. The PAN mesh was initially stabilized in the air by heating it to 250 °C at a rate of 1 °C minand maintaining that temperature for one hour. The stabilized PAN nanofibers were subsequently heated in a furnace at a rate of 5 °C min⁻¹ to 1000 °C and carbonized in a nitrogen atmosphere at 1000 °C for one hour. Then, solid KOH (Fisher Scientific) was pulverized with the carbonized PAN fibers at a weight ratio of 3:1. The mixture was heated to 1000 °C at a rate of 5 °C min⁻¹ and maintained in a furnace with free-flowing N2 for one hour. Finally, the samples were lyophilized for future use after being dialyzed in deionized water to remove any remaining KOH. For the WiSE,

¹School of Engineering, Brown University, Providence, Rhode Island 02912, United States of America

²Department of Mechanical and Industrial Engineering, Northeastern University, Boston, Massachusetts 02115, United States of America

^{*}Electrochemical Society Student Member.

^{**}Electrochemical Society Member.

^zE-mail: changmin_shi@brown.edu; brian_sheldon@brown.edu

LiTFSI salt (99.99%, Sigma Aldrich) was dissolved in DI water. ¹⁹ The mixture had been stirred for \sim 8 h at room temperature before it was used as an electrolyte. In addition, the electrolyte-to-electrode weight ratio is 25: 1 to avoid limitations in ion availability.

Characterization.—The biochar Specific Surface Area (SSA) and porosity were investigated using an Autosorb-1 instrument (by Quantachrome Instruments, today Anton-Paar). In these experiments, approximately 40-80 mg of biochar was placed into sample glassware and outgassed at 200 °C for 24 h. The N₂ adsorption-desorption isotherms were obtained by recording data points at relative pressures (P/P_0) from 10^{-6} to 1 at a temperature of 77 K. The SSA values were calculated by applying the Brunauer-Emmett-Teller (BET) model and the pore size distributions using the non-local density functional theory (NLDFT) slit pore model.²³ The pore sizes are presented according to the International Union of Pure and Applied Chemistry (IUPAC) classification, which defines pores less than 2 nm wide as micropores, pores with widths between 2-50 nm as mesopores, and pores wider than 50 nm as macropores. Micropore volume and micropore SSA were also determined by applying the Dubinin-Radushkevitch (DR) theory. The morphology of the all-biomass electrodes was characterized by Environmental Scanning Electron Microscopy (SEM, Thermo Scientific Ouattro S) with a voltage of 5 kV. For Energy Dispersive X-ray (EDX) Analysis shown in Figs. S5 and S6, and Tables S1 and S2, a voltage of 20 kV was applied to ensure good EDX signals.

Supercapacitor cell assembly and testing.—Swagelok cells (X2 lab) were employed for cell assembly. The cell configuration within the Swagelok cell is: electrode/electrolyte + glass fiber separator (Tisch Scientific) + electrolyte/electrode. For the conventional aqueous electrolyte used in this work is 6 M KOH (Lab Alley Essential Chemicals). The cells were rest for overnight before any electrochemical measurements. All the electrochemical tests were conducted by using a Bio-logic VSP-300 potentiostat. For Cyclic Voltammetry (CV) scanning, the voltage range was set to be either 0 V to 3 V for electrodes using WiSE or 0 V to 0.8 V for electrodes using 6 M KOH aqueous electrolyte, with different voltage scanning rates. The cell configuration during the CV measurements was the following: our-designed-electrode/WiSE or 6 M KOH aqueous electrolyte/our-designed-electrode. Such cell configuration was followed by the past published results.^{25,26} For the Electrochemical Impedance Spectroscopy (EIS) tests, the frequency was from 1 MHz to 0.1 Hz with a voltage amplitude of 10 mV. For the Distribution of Relaxation Times (DRT) analysis (Fig. S4), the Gaussian discretization method was applied²⁷ with a regularization parameter of 1 to minimize the data noise in the EIS measurement. Furthermore, the regularization derivative is first order.

For the capacitance evaluation and long-term cycling tests, the voltage cutoff was set between -3~V to +3~V and -0.8~V to +0.8~V for the cells using WiSE and 6~M KOH aqueous electrolyte, respectively. For capacitance, areal energy density, and power density evaluation, the current densities were set to be $5~mA~cm^{-2}, 10~mA~cm^{-2}, 15~mA~cm^{-2}, and <math display="inline">30~mA~cm^{-2}.$ For the long-term cycling tests, the current density was set to be $10~mA~cm^{-2}.$

Energy density and power density calculation.—Energy density (*E*, mWh cm⁻²) was calculated as:

$$E = \frac{0.25CV^2}{3600}$$

where C and V are the areal discharge capacitance (mF cm⁻²) and voltage cutoff (3 V), respectively.

Power density $(P, \text{ mW cm}^{-2})$ was calculated as:

$$P = \frac{3600E}{t}$$

where t is the discharge time per half cycle.

Note that for both energy density and power density calculations, including the values extracted from the literature, we based our calculations on the electrode level. Packaging materials and electrolytes were not considered in these calculations.

Results and Discussion

SSA and specific pore sizes are essential factors on storing charges for the supercapacitor. A larger SSA with specific pore sizes can provide more active sites for ion adsorption, leading to higher charge storage capacity. It is not the SSA alone, but also specific porosity that can significantly impact ion transport and storage mechanisms. 28,29 The surface morphology, SSA and Pore Size Distribution (PSD) were determined for biomass supercapacitor electrode. The representative SEM images and the N₂ adsorption isotherm obtained at 77 K together with the PSD are shown in Fig. 1. The SEM images of the top view and cross-sectional view of the allbiomass electrode show similar surface features in terms of SSA and porosity (Figs. 1a and 1b), indicating uniformity throughout the thick electrode. The Brunauer-Emmett-Teller (BET) SSA obtained from the N_2 adsorption isotherm (Fig. 1c) is $464 \text{ m}^2 \text{ g}^{-1}$. According to International Union of Pure and Applied Chemistry classification the all-biomass electrode N₂ isotherm can be categorized as type 1 adsorption isotherm. The type 1 adsorption isotherms feature a steep rise at relative pressures (P/P_o) below 0.1. After the relative pressures of 0.1, the N₂ isotherm has fairly mild slope upwards towards N₂ saturation, which is an indicative of some mesoporosity in this biomass electrodes samples. 30,31 The PSD shown on Fig. 1d confirms these findings. The majority of pores available in these biochars are indeed micropores (pores and cavities below 2 nm in size). The PSD in Fig. 1d confirms that there is also some mesoporosity (pores or cavities above 2 nm) in this all-biomass electrode.

This combined features led to a wide presence of micropores and macropores. 30,31 In addition, there are some slit pores 24 in the electrodes (Fig. S1), but it did not lead to any hysteresis in the BET curve. Overall, although the SSA of the all-biomass electrode can be further expanded via alternative activation routines, it is already comparable and even beyond with the state-of-art biomass-based electrodes $(0.15-419~{\rm m}^2~{\rm g}^{-1})$. $^{32-35}$ The pore size distribution of the designed all-biomass electrode was shown in Fig. 1d. It suggested that most of the pore were between 2.5 and 4.5 nm in size. These small pore sizes can provide large number of active sites to store charges. $^{36-38}$ In addition, to broaden the application of WiSE for supercapacitor, an alternative supercapacitor electrode—PPCF with a SSA of 1519 m² g $^{-1}$ and pore size predominately smaller than ten angstroms 21,22 was employed which has been characterized in our previous publications.

From electrochemical aspect, CV scanning (Fig. 2) was first conducted to evaluate the stability of WiSE (Water-in-Salt Electrolyte) across a wide voltage window (3 V vs reference electrode) and the electrode-WiSE interfacial stability. For both all-biomass electrode and PPCF electrode, the results showed that WiSE is not electrochemically decomposed across the wide voltage window of 3 V (Figs. 2 and S2). The very first half cycle of the CV measurements at different voltage scanning rates is regarded as a linear sweep voltammetry test. The CV scanning results indicate that this highly concentrated electrolyte effectively inhibits undesirable water-splitting reactions. 18 From the perspective of electrode-WiSE interfacial stability, the CV scans revealed the presence of a faradaic charge transfer and storage process for both types of electrodes, suggesting pseudocapacitance behavior. Such pseudocapacitive behavior led to higher capacitance compared to purely electrostatic double-layer capacitance. 39 The pseudocapacitance behavior was especially evident (yellow rectangles in Figs. 2a and 2c) between 2.0 V and 3.0 V at lower scan rates (e.g., 5 mV s⁻¹). Note that, this interesting and excellent pseudocapacitive behavior is likely due to the superficial oxygen functional groups formed in the electrodes, 21,40 which is achieved here without introducing any

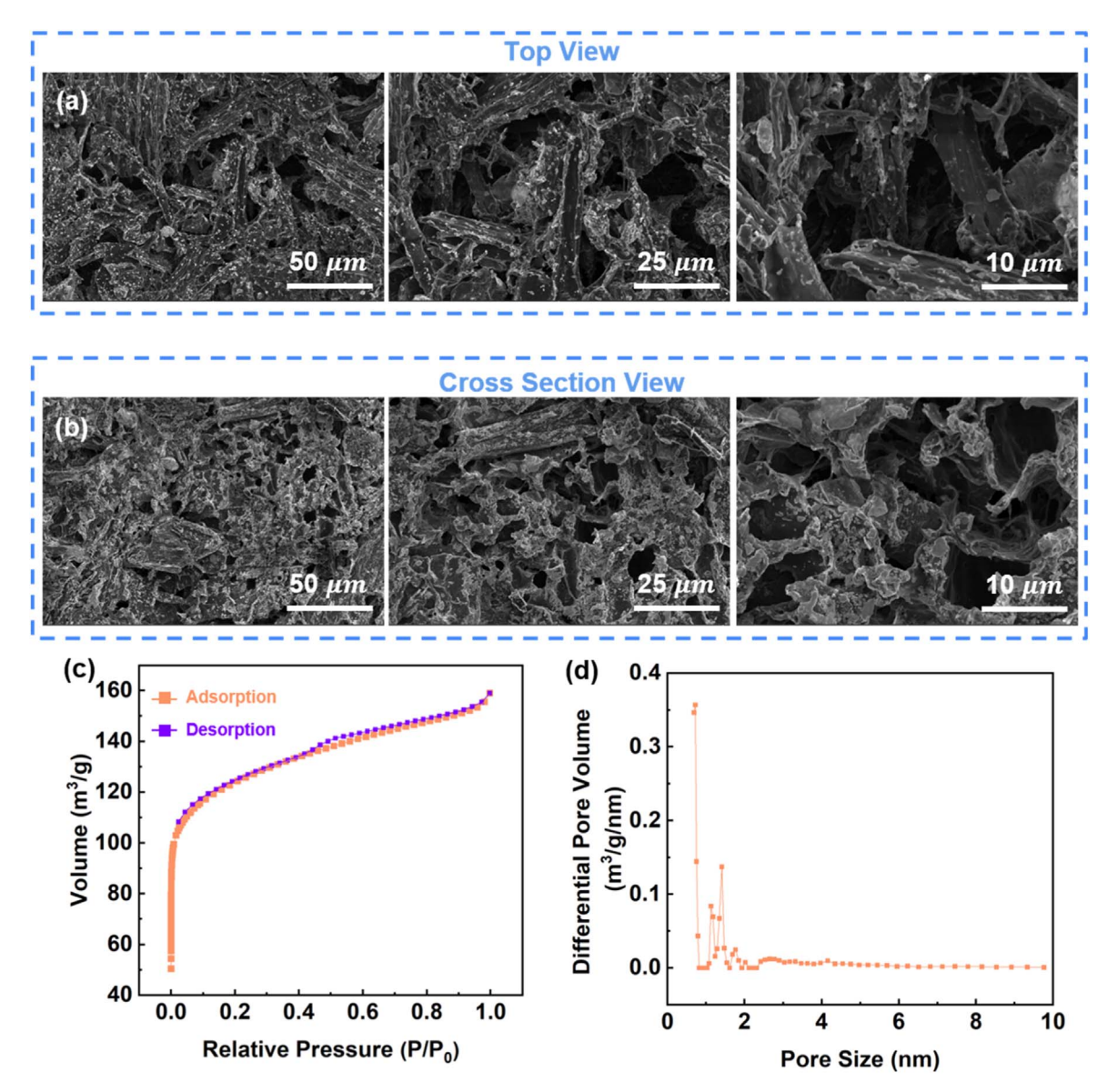


Figure 1. Characterization of the designed all-biomass supercapacitor electrode. (a). and (b). SEM images of the designed all-biomass electrode from the top view and cross section view, respectively. (c). A representative N_2 adsorption/desorption isotherm obtained at 77 K, providing the BET SSA of 464 m² g⁻¹, and (d). A representative pore size distribution of the designed all-biomass electrode.

additive chemistry. The possible faradic reactions occur in the system can be: (i). surface redox (e.g., non-diffusion limited reaction) reaction at the electrode surface areas;²¹ (ii). partial intercalation of the Li-ion in the carbon host electrodes. In contrast, published results employed additives (e.g., polypyrrole) to induce such pseudocapacitive behavior. The pseudocapacitive behavior disappears at higher voltage scanning rates due to the sluggish reaction kinetics, where the redox processes cannot keep up with the rapid voltage changes.⁴³ By comparing these two electrodes, the all-biomass electrode (Figs. 2a and 2b) showed a more resistive capacitor behavior (Figs. 2b and 2d), This difference is mainly attributed to the higher mass loading of the all-biomass electrode, which is 95 mg cm⁻², more than ten times higher than the mass loading of the PPCF electrode at 7.5 mg cm⁻². High mass loading leads to increased resistance within the electrode. Furthermore, the pseudocapacitance behavior was not observed when 6 M KOH aqueous electrolyte was used (Fig. S3). The results indicate that WiSE shows great promise for high-voltage supercapacitor design when combined with our two types of electrodes. The ability of WiSE to maintain electrochemical stability across a wide voltage window and support pseudocapacitance behavior is

particularly advantageous. Pseudocapacitance can enhance the energy storage capacity of supercapacitors by providing additional faradaic charge storage mechanisms beyond the simple electrostatic interactions found in electric double-layer capacitors.

Next, areal discharge capacitance, energy density, and power density of both types of electrodes was evaluated at different current densities (Fig. 3). Given the high mass loading of the all-biomass electrode, it showed a larger areal discharge capacitance at various current densities. Specifically, the areal discharge capacitance was 3107 mF cm^{-2} and 807 mF cm^{-2} at 5 mA cm^{-2} and 30 mA cm^{-2} , respectively (Fig. 3a). The areal discharge capacitance of the PPCF electrode showed a discharge capacitance of $677~\mathrm{mF\,cm^{-2}}$ and $204~\mathrm{mF\,cm^{-2}}$ at $5~\mathrm{mA\,cm^{-2}}$ and $30~\mathrm{mA\,cm^{-2}}$, respectively (Fig. 3c). However, the high mass loading (95 mg cm^{-2}) of the all-biomass electrode resulted in a relatively larger voltage drop due to ohmic loss (Fig. 3b) compared with the PPCF electrode (Fig. 3d). For example, the voltage drop was $\sim 0.65 \text{ V}$ at the starting point of the discharge process at a current density of 5 mA cm⁻². In addition, the voltage profiles at a relatively low current density of 5 mA cm⁻² showed a nonlinear shape (Figs. 3b and 3d), which can be attributed to pseudocapacitance behavior involving a faradaic type of charge

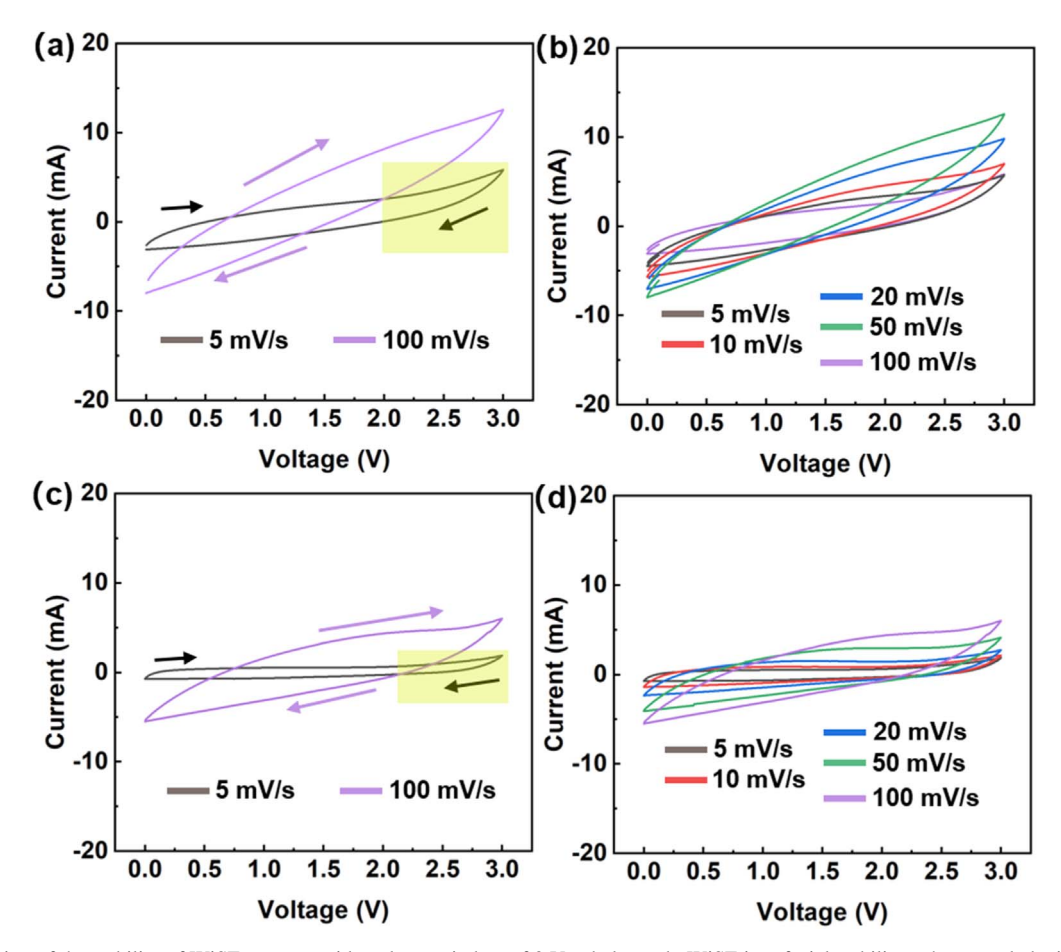


Figure 2. Evaluation of the stability of WiSE across a wide voltage window of 3 Vand electrode-WiSE interfacial stability, when coupled with the two types of electrodes. (a) and (b) CV scan of the designed all-biomass electrode at different voltage scanning rates. (c) and (d) CV scan of the designed PPCF electrode at different voltage scanning rates.

storage process. This observation is in good agreement with the CV scan results (Fig. 2). At higher current densities (e.g., $>10~\text{mA}~\text{cm}^{-2}$), the voltage profiles for both electrodes showed a linear character, suggesting the common electric double-layer capacitive behavior that is governed by the electrostatic accumulation of charge at the electrode-electrolyte interface.

Based on the achieved areal discharge capacitance, the areal energy density (mWh cm⁻²) and power density (mW cm⁻²) at an electrode level were evaluated and compared with state-of-the-art results in the supercapacitor field, where electrodes are made of biomass and carbon-based materials.^{22,44–52} Figure 3e shows that both types of electrodes, especially the all-biomass electrode, exhibited excellent areal energy density in the supercapacitor field when employed with WiSE. Despite the pseudocapacitance behavior seen in Fig. 2, areal power density remained great. Specifically, the highest areal energy density and power density achieved by the all-biomass electrode were up to 2.2 mWh cm⁻² and 11.7 mW cm⁻², respectively. The highest areal energy density and power density achieved by the PPCF electrode were up to 0.4 mWh cm⁻² and 12.1 mW cm⁻², respectively.

Finally, the EIS data of the supercapacitor cells are summarized in Fig. 4a, and the long-term cycling performance was evaluated. It shows that the baseline cell using the all-biomass electrode and 6 M KOH aqueous electrolyte had the lowest ASR of $\sim\!0.2$ ohm-cm². In contrast, the cells using the all-biomass electrode and WiSE showed ASR of $\sim\!4.1$ ohm-cm², while the cells using the PPCF electrode and WiSE showed ASR of $\sim\!6.6$ ohm-cm². Comparing the ASR in cells with all-biomass electrodes using WiSE and 6 M KOH aqueous electrolyte, the increased total ASR can be attributed to the high concentration of the Li salt and the formation of a LiF passivation

layer, ^{53–55} despite an expanded electrochemical stability window. It should be noted that with WiSE, the cells using the PPCF electrode showed a 1.5 times higher ASR than those using the all-biomass electrode. This can be attributed to the large SSA of the PPCF electrode, leading to a greater amount of LiF passivation layers.

For the cells made with all-biomass electrodes, despite a relatively larger ASR when using WiSE compared to conventional 6 M KOH aqueous electrolyte, the cell showed excellent cycling stability, especially after the 325th cycle (Fig. 4b). The areal discharge capacitance stabilized at ~1590 mF cm⁻². Similar capacitance decay-stabilization behavior by using concentrated aqueous electrolyte has been observed by Quan et al.⁵⁶ While for the cell using 6 M KOH aqueous electrolyte, the discharge capacitance continuously decreased without stabilization. By comparing these two cases, we believe the continuous capacitance fading in the baseline cell may be attributed to side reactions occurring between the all-biomass electrode and 6 M KOH aqueous electrolyte, which continuously reduces the active sites within the electrode and consumes the salt in the aqueous electrolyte. For the WiSE case, the LiF generated from the formation of solid electrolyte interphase (SEI) at the electrode-WiSE interface may block some active sites in the all-biomass electrode and reduce charge storage kinetics. For example, the DRT analysis for the all-biomass electrode coupled with WiSE (Fig. S4) shows that the charge storage kinetics is the primary limiting factor in achieving higher power density for our design at low characteristic frequencies (or within the high relaxation time domain, 400-500 s). However, the formation of LiF preented further electrode-electrolyte interfacial reactions. 18,56,57 This resulted in an initial reduction in discharge capacitance followed by stabilization. The formation of the LiF passivation

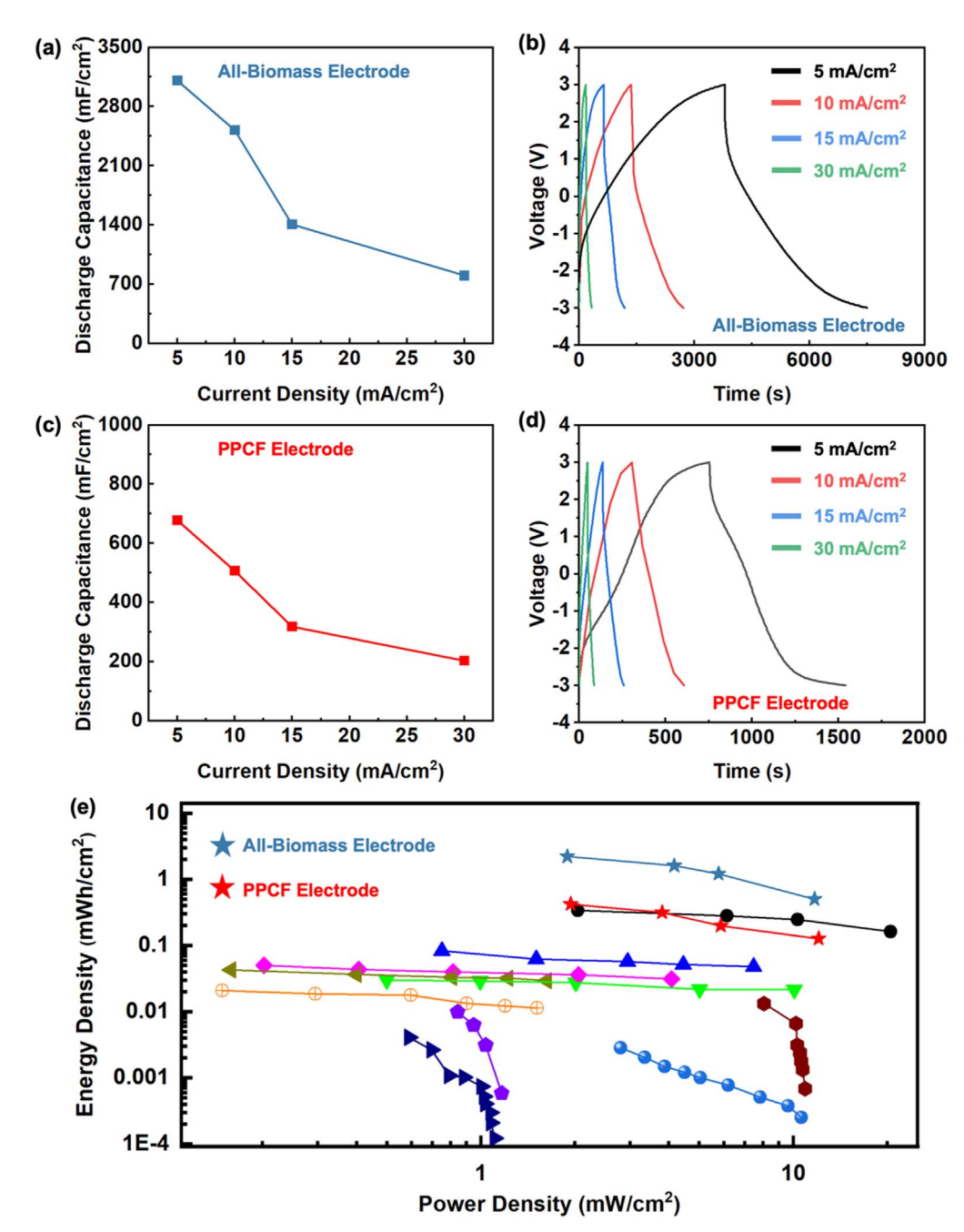


Figure 3. Areal capacitance, energy density and power density evaluations. (a). and (b). Areal capacitance evaluation under different current density for the designed all-biomass electrode and PPCF electrode, respectively. (c). and (d). Voltage profile of the designed all-biomass electrode and PPCF electrode, respectively, at different current density. (e). Ragone plot for areal energy density and power density comparison. Except for the star marks values which come from the electrodes used in this work, all other data points were extracted from published results. ^{22,44–52} All the tests were performed at room temperature.

layer at the electrode-electrolyte interface needs careful consideration to balance charge storage kinetics and interface stability. However, further investigation is necessary to fully understand the capacitance decay and stabilization mechanisms. For the cell using the PPCF electrode and WiSE, it showed a stabilized areal discharge capacitance of $\sim\!503\,\mathrm{mF\,cm^{-2}}$ in the first 70 cycles, although it decayed relatively slowly in the following cycles. One possible reason is that, for the PPCF electrode, its larger surface area (compared with the all-biomass electrode) leads to a larger decomposition of WiSE at the electrode-electrolyte interface, thus consuming more Li salt. This is consistent with the observation that the PPCF electrode shows more fluorine decomposition after long-term cycling, compared with the all-biomass electrode (Figs. S5 and S6, and Tables S1 and S2). This larger Li salt consumption then leads to more ion depletion in the WiSE. Therefore,

the number of ions that can be stored is fewer. Furthermore, with the large surface area in PPCF electrode, the entire electrode-electrolyte interface would be impossible to be fully passivated and stabilized. This leads to a continuous consumption of ions in the WiSE, resulting in a continuous capacitance delay. In addition, the gradual capacitance decay over extended cycles has been observed in our previous publication at a current density of 5 mA cm⁻² with a mass loading of 10 mg cm⁻² by using a different electrolyte chemistry, ²² and we believe that the discharge capacitance can be further stabilized by improving the engineering-level electrode synthesis. Comparing the all-biomass electrode and the PPCF electrode capacitance retention behavior (Fig. 4b) over an extended period, suggests that a balanced surface area and the formation of LiF is very important to maintain a high capacitance stabilization.

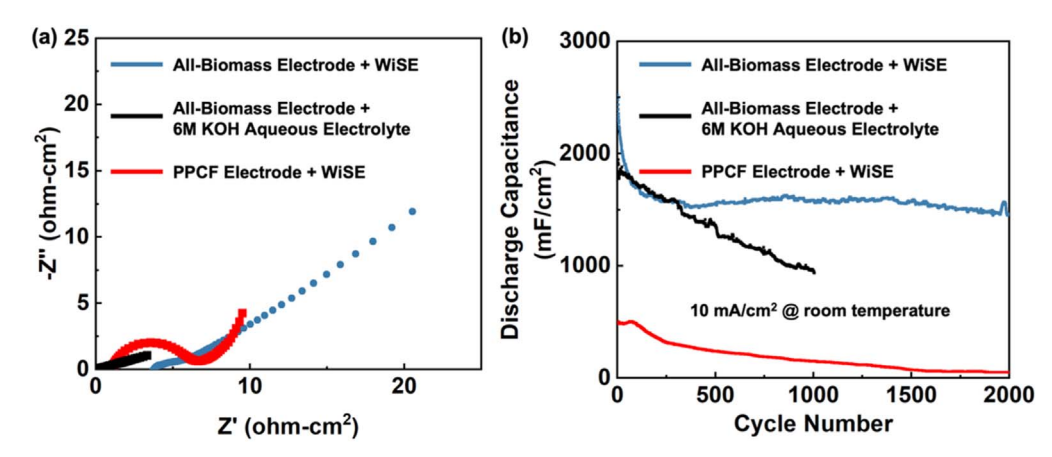


Figure 4. Supercapacitor long-term cycling performance under different conditions. (a). EIS data of supercapacitors by using an all-biomass electrode and PPCF electrode with different electrolytes. (b). Long-term cycling evaluation for the designed all-biomass electrode and PPCF electrode at a current density of 10 mA cm⁻² at room temperature.

Conclusions

This work demonstrates the potential of using a WiSE to achieve a high-voltage supercapacitor with carbon-based electrodes, while also providing insights into the electrochemical phenomena observed. Both the all-biomass and PPCF electrodes can operate effectively with WiSE across a wide voltage window of 3 V, inhibiting undesirable water-splitting reactions. The presence of pseudocapacitance behavior, as evidenced by CV scans, contributed to higher charge storage capacity. Consequently, a high areal energy density and power density of 2.2 mWh cm⁻² and 11.7 mW cm⁻³ were achieved for the all-biomass electrode, and a high areal energy density and power density of 0.4 mWh cm⁻² and 12.1 mW cm⁻² were achieved for the PPCF electrode. Additionally, although the all-biomass electrode showed a relatively larger ASR with WiSE compared to conventional 6 M KOH aqueous electrolyte, it maintained excellent cycling stability, which is possibly due to the generation of a passivating SEI layer that protects the electrodeelectrolyte interface. The findings suggest that WiSE has great promise for the development of high-voltage carbon-based supercapacitors, offering a balanced approach to optimizing charge storage kinetics and interface stability.

Acknowledgments

The authors would also like to thank Dr Zachary Saleel for helping coordinate with SSA and specific pore size distribution measurements.

ORCID

Changmin Shi https://orcid.org/0000-0003-1978-7352 Brian W. Sheldon https://orcid.org/0000-0002-9593-891X

References

- 1. L. Zhang, X. Hu, Z. Wang, F. Sun, and D. G. Dorrell, Renew. Sustain. Energy Rev.,
- X. Yang, T. Lv, and J. Qiu, Small, 19, 1 (2023).
- 3. X. Zhang et al., Chem. Eng. J., 460, 141607 (2023).
- 4. C. Shi et al., ACS Appl. Mater. Interfaces, 15, 751 (2023).
- 5. J. Zhang, M. Gu, and X. Chen, *Micro Nano Eng.*, 21, 100229 (2023).
- 6. P. Sharma and V. Kumar, J. Electron. Mater., 49, 3520 (2020).
- 7. D. B. Basha, S. Ahmed, A. Ahmed, and M. A. Gondal, J. Energy Storage, 60, 106581 (2023).
- 8. P. A. Shinde et al., J. Energy Chem., 79, 611 (2023).
- 9. K. C. S. Lakshmi and B. Vedhanarayanan, Batteries, 9 (2023), https://mdpi.com/ 2313-0105/9/4/202
- 10. P. Azaïs et al., J. Power Sources, 171, 1046 (2007).
- 11. J. W. Long et al., MRS Bull., 36, 513 (2011).
- 12. H. Zhang, X. Liu, H. Li, I. Hasa, and S. Passerini, Angew. Chemie Int. Ed., 60, 598 (2021).

- 13. C. Zhong et al., Chem. Soc. Rev., 44, 7484 (2015).
- A. Ray and B. Saruhan, *Materials (Basel).*, **14** (2021), https://mdpi.com/1996-1944/
- 15. T. Abdallah, D. Lemordant, and B. Claude-Montigny, J. Power Sources, 201, 353 (2012)
- 16. C. Shi and M. Yu, Energy Storage Mater., 57, 429 (2023).
- 17. C. Shi et al., ACS Energy Lett., 8, 1803 (2023).
- 18. L. Suo et al., Science (80-.)., 350, 938 (2015).
- 19. X. Tian, Q. Zhu, and B. Xu, Chem. Sus. Chem, 14, 2501 (2021).
- 20. Q. Zhang et al., Energy Storage Mater., 55, 205 (2023).
- 21. X. Sun et al., Small, 18, 1 (2022).
- 22. Y. Wang, Z. Wei, T. Ji, R. Bai, and H. Zhu, Small, 20, 1 (2024).
- 23. C. Lastoskie, K. E. Gubbins, and N. Quirked, J. Phys. Chem., 97, 4786 (1993).
- 24. S. Lowell, J. Shields, M. Thomas, and M. Thommes, Characterization of Porous Solids and Powders: Surface Area, Pore Size and Density (Springer Netherlands, Dordrecht) (2006), https://link.springer.com/book/10.1007/978-1-4020-2303-3.
- B. Jinisha et al., J. Solid State Electrochem., 23, 3343 (2019).
- Y. Huang et al., ACS Appl. Mater. Interfaces, 8, 15205 (2016).
- 27. T. H. Wan, M. Saccoccio, C. Chen, and F. Ciucci, *Electrochim. Acta*, **184**, 483 (2015).
- 28. P. De et al., *Electrochem. Sci. Adv.*, 3, 1 (2023).
- P. De et al., Electrochem. Sci. Natr., 5, 1 (2023).
 Z. Supiyeva, X. Pan, and Q. Abbas, Curr. Opin. Electrochem., 39, 101249 (2023).
 Z. A. Alothman, Materials (Basel)., 5, 2874 (2012).
- 31. J. Rouquerol et al., Pure Appl. Chem., 66, 1739 (1994). 32. B. Rui et al., J. Appl. Electrochem., 50, 407 (2020).
- 33. J. Jiang, J. Electrochem. Soc., 164, H5043 (2017).
- 34. J. Jiang et al., *Electrochim. Acta*, 113, 481 (2013).
- 35. Z. W. Ma, H. Q. Liu, and Q. F. Lü, *J. Energy Storage*, 40, 102773 (2021).
- G. Pognon, T. Brousse, and D. Bélanger, Carbon N. Y., 49, 1340 (2011).
- 37. X. Li, Z. Su, P. Liang, and J. Zhang, Biomass Convers. Biorefinery, 13, 6237 (2023)
- 38. N. Boulanger, A. V. Talyzin, S. Xiong, M. Hultberg, and A. Grimm, Colloids Surfaces A Physicochem. Eng. Asp., 680, 132684 (2024).
- 39. P. Simon and Y. Gogotsi, Nat. Mater., 7, 845 (2008).
- 40. K. Gajewska, A. Moyseowicz, D. Minta, and G. Gryglewicz, J. Mater. Sci., 58, 1721 (2023).
- 41. D. Majumdar, J. Electroanal. Chem., 880, 114825 (2021).
- 42. N. Kamboj and R. S. Dey, Electrochim. Acta, 421 (2022), https://www.sciencedirect.com/science/article/pii/S0013468622006582
- 43. B. E. Conway, Electrochemical Supercapacitors Scientific Fundamentals and Technological Applications (1999), 1st ed. 1999. New York, NY (Springer US: Imprint: Springer, New York) 1999, https://search.library.wisc.edu/catalog/ 9913310453502121.
- Y. Shi et al., Chem. Eng. J., 392, 123645 (2020).
- R. Wang et al., Compos. Part B Eng., 275, 111345 (2024).
- 46. Z. Yong et al., J. Alloys Compd., 893, 162197 (2022).
- 47. S. Zheng et al., J. Mater. Chem. A, 7, 9478 (2019).
- Y. Shi, Y. Zhang, L. Jia, Q. Zhang, and X. Xu, ACS Appl. Mater. Interfaces, 10, 36028 (2018).
- 49. K. Wang et al., Adv. Mater., 27, 7451 (2015).
- 50. B. Asbani et al., J. Electrochem. Soc., 167, 100551 (2020).
- 51. C. Jin et al., *Electrochim. Acta*, 270, 205 (2018).
- 52. P. Pazhamalai et al., Adv. Mater. Interfaces, 5, 1 (2018).
- 53. A. Guha and T. N. Narayanan, JPhys Energy, 2 (2020), https://iopscience.iop.org/ article/10.1088/2515-7655/ab8e25/meta
- 54. C. Shi et al., Adv. Energy Mater., 13, 2301656 (2023).
- 55. P. Lannelongue et al., J. Electrochem. Soc., 165, A657 (2018).
- 56. T. Quan et al., ACS Appl. Mater. Interfaces, 13, 3979 (2021).
- 57. S. Lindberg et al., Batter. Supercaps, 3, 1233 (2020).